Fast post-processing pipeline for optical projection tomography

Tang, X.; Zwaan, D.M. van der; Zammit, A.; Rietveld, K.F.D.; Verbeek, F.J.

Fast Post-Processing Pipeline for Optical Projection Tomography

Xiaoqin Tang, Dennis M. van der Zwaan, Alan Zammit, Kristian F. D. Rietveld, and Fons J. Verbeek

***Abstract*— To improve the effectiveness and efficiency of optical projection tomography (OPT) 3-D reconstruction, we present a fast post-processing pipeline, including cropping, background subtraction, center of rotation (COR) correction, and 3-D reconstruction. Regarding to the COR correction, a novel algorithm based on interest point detection of sinogram is proposed by considering the principle of OPT imaging. Instead of locating the COR on single sinogram, we select equally spaced sinograms in the detected full range of specimen to make the located COR more convincing. The presented post-processing pipeline is implemented in a parallel manner and the experiments show that the average runtime for each image of size 1036 × 1360 × 400 pixels is less than 1 min. To quantify and compare the reconstructed results of different COR correction approaches, the coefficient of variation instead of variance is employed. The results indicate that the proposed COR correction outperforms the three traditional COR alignment approaches in terms of effectiveness and computational complexity.**

***Index Terms*— OPT, COR correction, artifacts, 3D reconstruction, parallel computing.**

I. Introduction

MOLECULAR imaging as a direct visualization technology in cells, tissues and organs, is making a tremendous impact on biology and medical research. Genetic engineering technologies such as *in situ* hybridization as well as fluorescence staining permit the qualitative, quantitative and positioning analysis of protein and gene expression pattern in transgenic animals and plants. In the last two decades, studies of disease mechanisms and drug discovery have benefitted from high-resolution fluorescence microscopy techniques for instance confocal microscopy or multiphoton laser scanning microscopy (LSM), which enables the visualization of cell signaling networks [1], [2]. However, with the high-resolution imaging at cell level they are not suitable for larger specimen (∼0.5-10 mm scale) requiring larger fields of view and enormous imaging time consumption. Furthermore, due to the increasing evidence that mono-layer cell cultures may exhibit non-physiological behavior within the artificially planar environment, the trend from *in vitro* to *in vivo* contributes to an increasing change from the cellular scale to tissue scale or even whole organism [3], [4].

OPT, proposed by Sharpe *et al.* in 2002 [5], is one of the more popular instruments for imaging biological samples on the level of tissue, organ and organism. As a microscopy, OPT is relatively new; though it successfully fills the size gap between confocal microscopy [6] and magnetic resonance imaging (MRI) [7]. OPT allows for the acquisition of high resolution full body images of animal/plant tissues as well as animal organs/organisms [8], [9]. From evaluations OPT imaging has shown great potential with respect to high spatial resolution, contrast and minimal shadowing artifacts using back-projection reconstruction from multi-angle acquisition. In the recent years, cancer progression [10]–[12], drug discovery [13] and development studies such as skeleton [14], [15], teeth [16] and blood vessels [17] have profited from the growth of OPT microscopy. Kumar *et al.* [10] applied OPT to adult zebrafish for studying the cancer progression and vasculature development synchronously. McGinty *et al.* [13] proposed a fluorescence lifetime optical projection tomography in 2011 for biological research and drug discovery, but the time necessary for image acquisition and 3D reconstruction were both approximately 20 minutes. Later in 2012, Fieramonti *et al.* [14] extended OPT to optically diffusive samples for studying skeletal and nervous structures of zebrafish, improving the acquisition time as approximately 3 minutes but without considering the artifacts produced when the COR is inconsistent with the center of image. Agarwal *et al.* [12] presented a diagnosis method of early cancer by reconstructing the 3D cellular image with OPT in 2014. The high resolution of single cells was achieved by setting large numerical aperture (NA) and scanning the objective focal plan contributed to the extension of depth of field (DOF), which consequently increased the light dose and acquisition time. More recently in 2015, Correia *et al.* [17] introduced accelerated OPT by decreasing the number of rotations when imaging, aiming to improve the efficiency of OPT system and decrease the light dose.

With the same aim of improving the efficiency of OPT imaging, in a parallel manner, we present a fast OPT post-processing pipeline which contains preprocessing, COR correction and 3D reconstruction taking approximately 1 minute with an image size of $1036 \times 1360 \times 400$ pixels. In this manner,

Manuscript received May 7, 2017; accepted May 12, 2017. Date of publication May 23, 2017; date of current version August 11, 2017. The work was supported by China Scholarship Council. *(Corresponding author: Xiaoqin Tang.)*

The authors are with the Leiden Institute of Advanced Computer Science, Leiden University, 2333CA Leiden, The Netherlands (e-mail: x.tang@liacs.leidenuniv.nl; dennisvanderzwaan@hotmail.com; alanzammit@yahoo.co.uk; k.f.d.rietveld@liacs.leidenuniv.nl; f.j.verbeek@liacs.leidenuniv.nl).

Digital Object Identifier 10.1109/TNB.2017.2706967

we can make a quick assessment of the image quality so as to accept or reject the tomogram. Additionally, our pipeline facilitates fast processing of a large number of tomograms so that statistical distributions of our samples can be easily obtained.

Regarding to COR correction, when applying the inverse radon transform to 3D reconstruction, the COR position should be in the middle of the sinogram. This could be achieved by COR correction, which was first studied in 1990 [18] in computational tomography (CT). Previous studies showed that shifted COR could introduce severe artefacts or even incorrect results [19]. Furthermore, correcting COR based on images can bypass the hardware calibration before imaging, ameliorating the efficiency of the imaging system. In terms of COR correction methodologies, there are two mainstream approaches: the first approach is based on signal match for pairs of projection data (180 ° opposed to each other) [18], [20]–[22]. They are widely used in CT because the intensities from two opposite projected angles are theoretically equivalent in CT imaging. Unfortunately, these methods may not be suitable for OPT images, as opposite projected data vary differently at different angles. These differences are caused by the fact that OPT has a depth of focus (DOF) and only images the front half of the specimen [5]. Moreover the methods are not feasible when the sinogram is disturbed by fixed defects or random noise, which frequently occurs in OPT imaging. The second mainstream approach both for CT and OPT is based on iterative reconstruction in the sinogram [23]–[25]. The vertical axis producing the smallest variance in reconstructed image is chosen as the COR in [24]. However, this approach is time-consuming, making it seldom used in CT. Furthermore, both approaches choose only one sinogram for COR correction and the COR fluctuation produced by different sinograms was not taken into account, to some extent resulting inaccurate COR.

In our fast post-processing pipeline, cropping and background subtraction comprise the preprocessing of the images, followed by a new efficient COR correction algorithm, which significantly contributes to the innovation of our work. With the cropping and COR correction, the specimen can be placed at any position of the field of view (FOV), not only decreasing the time for post-processing of OPT but also avoiding the calibration process before imaging. Conventionally, the calibration helps to align the COR to the center of FOV, which normally takes several minutes. Besides the fast COR correction method, we implemented both COR correction and 3D reconstruction as parallel algorithms to further accelerate the post-processing of OPT, bringing each post-processing time down to approximately 1 minute.

This paper is organized as follows. Section 2 explains the OPT image data and post-processing pipeline, followed by the detailed introduction of the new COR correction algorithm. It also contains the 3D reconstruction and parallel implementation afterwards. Section 3 shows the experiment results of both reconstruction quality and runtime with the pipeline on different dataset as well as with different COR correction methods. Finally Section 4 presents our conclusion.

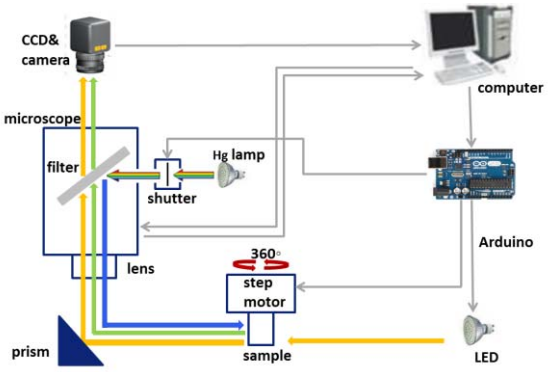

Fig. 1. Diagram of OPT imaging system. Hg lamp shows the illumination for fluorescence mode (fluorescence channel) and LED is for absorption mode (bright-field channel) in yellow. In fluorescence mode excitation and emission beams are shown in blue and green.

II. Material and Methodology

The OPT imaging system developed by our group support both absorption and fluorescence mode as shown in Fig. 1. The acquisition time of absorption mode is less than 3 minutes, and that of fluorescence mode varies depending on the fluorescence strength and exposure time but is typically less than 10 minutes for 400 images in full rotation. Optimization of sample preparation and image acquisition were implemented, but is not the focus of this paper. The raw data of the single channel from the OPT is a 16-bit high-resolution image of size $1036 \times 1360 \times 400$ pixels, with a file size of 1.05GB. 1036×1360 is the image size for one angle, and 400 is the number of rotation angles in [0°, 360°). In each mode, 10 background images with the same size of 1036×1360 are recorded for the post-processing.

With the post-procession pipeline, the acquired OPT images can be first cropped to locate the region of interest (ROI) for multiple channels if necessary, followed by the median background subtraction for each channel. Afterwards, COR correction as well as 3D reconstruction is performed. Specifically, CORs from different channels are located separately but aligned to the same reference before 3D reconstruction with inverse radon transform.

A. COR Correction

COR correction involves COR localization of each channel and COR alignment of multiple channels. Considering the artifacts from COR shift discussed in [25] and [26] and the computationally expensive problem of the traditional COR localization method by using iterative reconstruction [24], a novel COR localization approach is presented. The COR localization for each channel is defined as searching for the most frequently occurring value from the obtained CORs of multiple sinograms, which are localized based on interest point detection and COR optimization function.

1) Sinogram Selection: To make the COR localization of each channel convincing, multiple slices of sinogram are selected. Specifically, the slice range is first acquired asNS from 4 valid sinogram ranges using Eq. (1). NS_0, NS_{90}, NS_{180} and NS_{270} respectively represent the 4 slice ranges of 4 orthogonal projection images, as shown

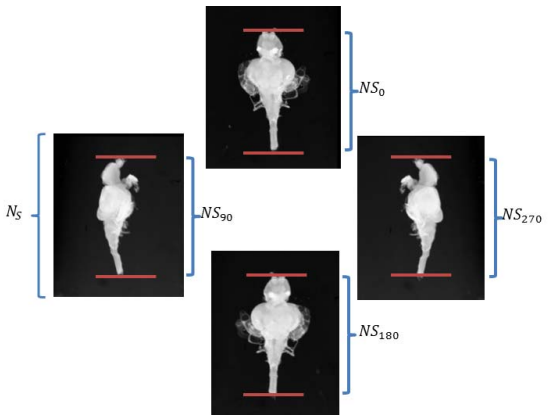

Fig. 2. The 4 orthogonal sinogram ranges NS_0, NS_{90}, NS_{180} and NS_{270} are from the 4 orthogonal projection images (0°, 90°, 180°, 270°) of zebrafish brain.

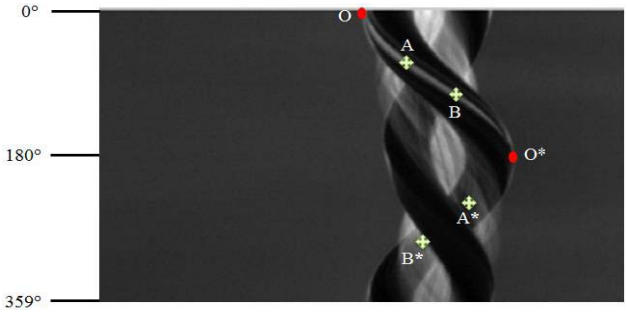

Fig. 3. One sinogram of the zebrafish embryo showing the differences among pairs of opposite projected data. O and O*, A and A*, B and B* are pairs respectively. O and O* are interest points; while A and A*, B and B* are not.

in Fig. 2.

$$NS = NS_0 \cap NS_{90} \cap NS_{180} \cap NS_{270} \tag{1}$$

Within NS, the step for selecting sinogram $step = ceil(\frac{NS}{\rho})$ is experimentally determined and approximately ρ sinograms from the range NS are evenly selected. The selected sinograms are defined as S. With this rule specimens have approximately the same number of selected sinograms for COR localization regardless of their different sizes. In Fig. 2 N_s is the full range of slices in 3D image after the cropping. In our case, N_s is 1360 without the cropping.

2) Interest Point Detection: According to the principle of our OPT imaging system, only the front half of specimen is in the DOF, so the projected data from opposite angles may vary differently depending on the rotation angle, specimen size and shape. However, a voxel projected at the left or right boundary of the specimen shares approximately the same image intensity with the opposite projection of the same voxel. This equivalence is shown as a peak and trough in the sinogram edge. To illustrate our hypothesis, a sinogram of the fluorescent channel of zebrafish larva is depicted as an example in Fig. 3. Point O, A and B are the fluorescence signals of the 6 dpf zebrafish eye from 3 different angles, and O*, A* and B* are their corresponding opposite projections. The projected data for an eye voxel should be formed as a sine function passing through O, A, B, O*, A* and B* in CT system, but in OPT only O and O* remain equivalent; while A and A* as well as B and B* differ significantly, being consistent with

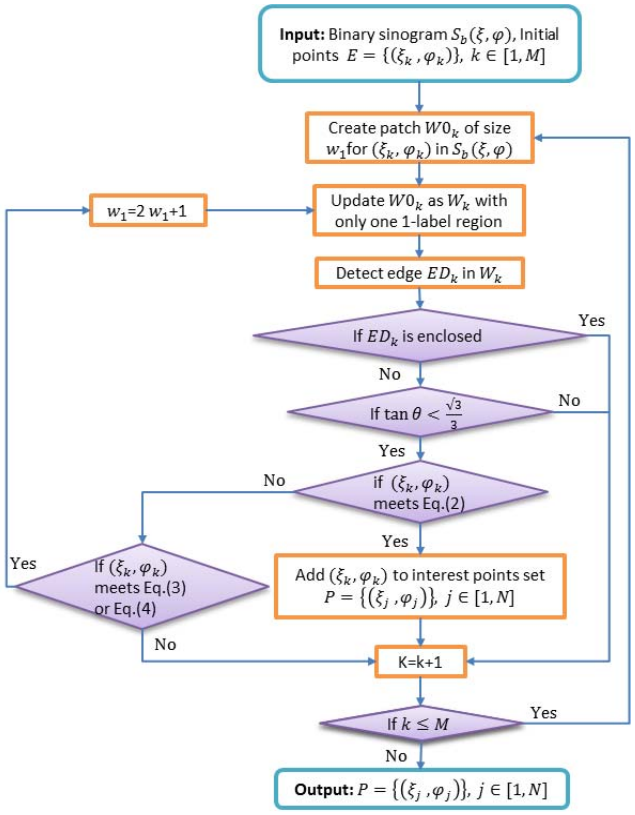

Fig. 4. Algorithm of interest point detection. Binary sinogram and initial points are obtained with OSTU [27] and Sobel edge detector [28] respectively.

the hypothesis above. With this hypothesis, the COR could be located with the oppositely projected pairs that are similar to O and O*. The problem of locating the COR is therefore transformed as search for peaks and troughs in the sinogram edge, in our case defined as interest points.

A sinogram is defined as $S(\xi,\varphi)$ with a size of$400\times p$ in our case, where φ is the rotating angle, and ξ is the phase in each angle. 400 is the image number for 360 angles and p is the cropped image size perpendicular to COR. As described in Fig. 4, the procedure of interest point detection is based on point selection with initial points $E=\{\xi_k,\varphi_k\}, k\in[1,M]$, the collection of points using edge detection in sinogram. $S_b(\xi,\varphi)$ refers to the binary sinogram. M is the number of initial points. After point selection, the detected interest points are $P=\{\xi_j,\varphi_j\}, j\in[1,N]$, and $N\le M$. The specific algorithm for point selection is depicted in Fig. 4.

Constrained by $\tan\theta < \frac{\sqrt{3}}{3}$ in Fig. 4, only points with $\theta < 30°$ remain. We define θ as the angle passing through the 0-labeled center $(\xi_{\text{zero}},\varphi_{\text{zero}})$ and the 1-labeled center $(\xi_{one},\varphi_{one})$ that are separated by edge ED_k in its patch W_k, instead of defining θ as the slope of ED_k. The peak and trough within W_k(red stars in Fig. 5) are defined as follows:

$$\text{Peak}: \begin{cases} \xi_{zero} > \xi_{one} \\ |D_\varphi| = (w_1 - 1) \\ D(D_\xi) < 0 \\ 1 \notin sign(d_{\xi 1}) \\ 1 \notin sign\left(d_{\xi 2}\right) \end{cases} \quad \text{Trough}: \begin{cases} \xi_{zero} < \xi_{one} \\ |D_\varphi| = (w_1 - 1) \\ D\left(D_\xi\right) > 0 \\ -1 \notin sign\left(d_{\xi 1}\right) \\ -1 \notin sign(d_{\xi 2}) \end{cases} \tag{2}$$

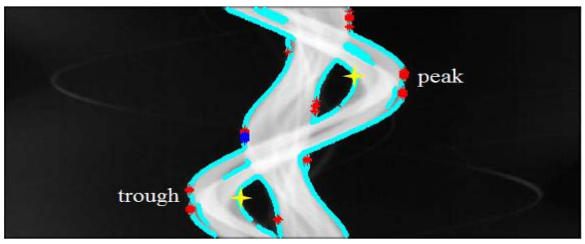

Fig. 5. One inverted bright-field sinogram from a chicken embryo heart images with interest points detected (shown as red and blue). Edge points (initial points) are shown as cyan points; while false-peak are shown as yellow cross.

D_φ symbolizes the sum of derivatives of ED_k in the φ direction along the edge curve, while $D(D_\xi)$ is the sum of second derivatives of ED_k in the ξ direction. When $D(D_\xi) < 0$, the function of ED_k sequence is constrained as convex, and if $D\left(D_\xi\right) > 0$ it is concave, corresponding to the peak and trough, respectively. We break ED_k into upper and lower edges: ED_{k1} and ED_{k2}, both of which are started at the middle of ED_k in the φ direction. $d_{\xi 1}$ and $d_{\xi 2}$ are the derivatives of ED_{k1} and ED_{k2} separately in the ξ direction.

With the definition in Eq. (2), false-peak and false-trough (yellow crosses in Fig. 5) are not kept as interest points, as they are not true sine peaks but rather intersections of different sine functions, which should be discarded. Furthermore, when a true trough satisfies Eq. (3) (blue star in Fig. 5):

$$\begin{cases} \xi_{zero} < \xi_{one} \\ |D_\varphi| = (w_1 - 1) \\ D\left(D_\xi\right) = 0 \\ sign\left(d_{\xi 1}\right) = 0 \\ sign\left(d_{\xi 2}\right) = 0 \end{cases} \tag{3}$$

or a true peak satisfies Eq. (4).

$$\begin{cases} \xi_{zero} > \xi_{one} \\ |D_\varphi| = (w_1 - 1) \\ D\left(D_\xi\right) = 0 \\ sign\left(d_{\xi 1}\right) = 0 \\ sign\left(d_{\xi 2}\right) = 0 \end{cases}, \tag{4}$$

It means that edge ED_k in W_k of size w_1 is strictly vertical, so it does not satisfy the definition of peak or trough in Eq. (2). The reason for this inconsistency comes from the size of W_k. To solve this problem, a bigger patch (set as $2w_1 + 1$ in our experiment) is set to satisfy Eq. (2) in a bigger patch, following the same interest point detection steps in Fig. 4.

3) COR Localization and Alignment: According to the definition of COR localization above, COR for single sinogram should be first localized. With the interest points $P = \left\{\xi_j, \varphi_j\right\}, j \in [1,N]$ detected in single sinogram, the COR range is obtained as $[\xi_{min}, \xi_{max}]$, where ξ_{max} and ξ_{min} are the maximum and minimum of ξ_j in the interest points P. For a specific COR c, we locate the corresponding opposite points for all the interest points P as $P_c^{'} = \{\left(\xi_j, \varphi_j\right)_c^{'}, j \in [1, N]$, which are symmetric by c and have an interval of 180° in projection. To find a mathematical metric between P and $P_c^{'}$, we define the neighbors of $\left(\xi_j, \varphi_j\right)$ and $\left(\xi_j, \varphi_j\right)_c^{'}$ as $r_c\left(\xi_j, \varphi_j\right)$ and $r_c^{'}(\xi_j, \varphi_j)$. As shown in Fig. 3, the projection data between interest point $\left(\xi_j, \varphi_j\right)$ and its opposite point $\left(\xi_j, \varphi_j\right)_c^{'}$ should be approximately equivalent,

so we localize the optimal COR in the range of $[\xi_{min}, \xi_{max}]$ for the ith sinogram by formulating Eq. (5).

$$C_i^* = \frac{1}{N}\sum_j^N \left(r_c\left(\xi_j, \varphi_j\right) - r_c^{'}(\xi_j, \varphi_j)\right) \tag{5}$$

For the selected ρ sinograms, the corresponding optimal CORs localized are $C = \{C_1^*, C_2^*, \ldots, C_\rho^*$. So the most frequently occurring value C^* in C is referred to as the COR for single channel.

For multiple channels the sinograms should be aligned to the same size with the same COR before 3D reconstruction, which may result from the tiny mechanic COR disparity when images are recorded at different times. We illustrate our alignment scheme in two channels (fluorescence and bight- field), which is also suitable to multiple channels. The ith sinogram S_i of size $400 \times p$ in each channel is aligned centred by C^* as $S_i^{'}$ of size $400 \times q$ by employing Eq. (6) and Eq. (7).

$$q = \begin{cases} 2 \times C^*, C^* < \frac{p}{2} \\ 2 \times (p - C^*), C^* \geq \frac{p}{2} \end{cases} \tag{6}$$

$$S_i^{'} = \begin{cases} S_i(1 : 2C^*, \varphi), C^* < \frac{p}{2} \\ S_i(2C^* - p : p, \varphi), C^* \geq \frac{p}{2} \end{cases} \tag{7}$$

As illustrated in Eq. (6), q is calculated to be smaller than p to preserve sufficient sinogram information, as well as to avoid redundant background reconstruction, i.e. S_i is truncated instead of being extended, which consumes more time for reconstructing the background. With Eq. (6) and Eq. (7), the ith sinogram for fluorescence and bright-field channel are $S_{fi}^{'}$ and $S_{bi}^{'}$ with size of $400 \times q_f$ and $400 \times q_b$ respectively. They are aligned to the same COR with the same size as S_{fi}^* and S_{bi}^* by using Eq. (8):

$$\begin{cases} S_{fi}^* = \left(z_0, S_{fi}^{'}, z_0\right); S_{bi}^* = S_{bi}^{'}, & q_f < q_b \\ S_{fi}^* = S_{fi}^{'}; S_{bi}^* = \left(z_0, S_{bi}^{'}, z_0\right), & q_f > q_b \end{cases} \tag{8}$$

Where z_0 is a zero matrix with size of $400 \times \left|C_f^* - C_b^*\right|$, and C_f^* and C_b^* represent the located CORs for the fluorescence and bright-field channel.

B. Reconstruction and Fusion

By applying inverse radon transform [29] to fluorescence and bright-field channel for specimens, the reconstructed images are formed as $R_f^t = \{R_{f1}, \ldots, R_{fl}, \ldots, R_{fL}$ and $R_b^t = \{R_{b1}, \ldots, R_{bl}, \ldots, R_{bL}$ respectively. L is the number of sinogams at imaging time t. The intensities in R_{fl} and R_{bl} refer to the fluorescence and bright-field signals. For the transparent specimens such as zebrafish larvae in our experiment, the bright-field signals are generally distributed in vertebral and bones, describing the zebrafish silhouette. Therefore, by fusing R_f^t and R_b^t, fluorescence signals for

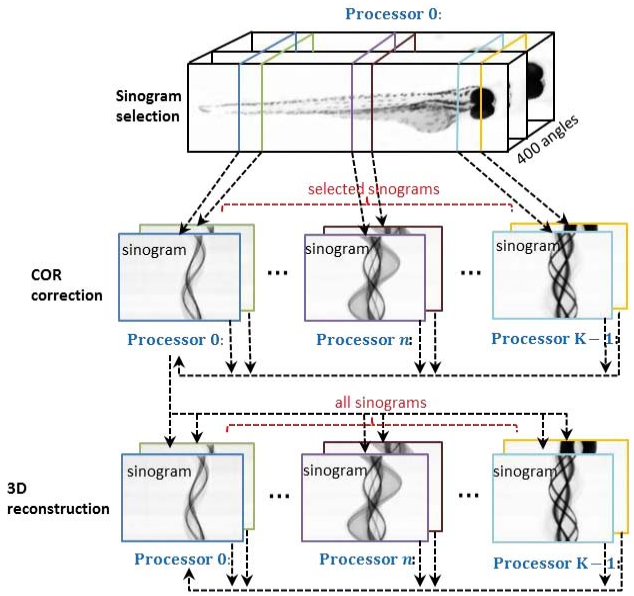

Fig. 6. Parallel framework for COR correction and 3D reconstruction. Processor 0 is defined as master node and is responsible for sinogram selection, broadcast and collective communication, as well as normalization before image writing.

instance gene expression pattern could be better located and analyzed within specimens at the specific time t. R_f^t and R_b^t are fused according to their equivalent slice number l and imaging time t. For each voxel in the fused 4D image, $V_{(x,y,l,t)} = (I_f, I_b)$ describes its signals of different channels, and (x, y, l, t) symbolizes the coordinate in 4D space. (x, y) corresponds to the pixel of the reconstructed image slice, while l and t symbolize the slice number and imaging time. $V_{(x,y,l,t)}$ could be further used for 3D segmentation and quantitative calculation of fluorescence labeling (gene and/or protein activity) in specimen or organs.

C. Parallel Implementation

We implemented COR correction and 3D reconstruction of the proposed pipeline as parallel algorithms. The specific implementation is illustrated in Fig.6. K is the number of available processors. Processor 0 is defined as Master responsible for sinogram selection, broadcast and collective communication. The selected sinograms S are then distributed to the K processors for localizing the corresponding CORs using Eq. (5). All the CORs from different processors are gathered by Master to calculate the C^* of each channel. Afterwards the COR alignment of different channels with Eq. (6), Eq. (7) and Eq. (8) is also implemented on Master. After COR correction, processor 0 distributes the L slices of aligned sinograms to the K processors for the 3D ronconstruction. The reconstructed results will be gathered again to processor 0 for normalizing pixel values to 0∼255 before image writting.

III. Experiment

A. Implementation of the Fast Post-Processing Pipeline

Without calibration of COR on hardware in the imaging system, we imaged a 3 dpf zebrafish and reconstructed it using the proposed pipeline. The raw 1036×1360×400 OPT image was first cropped manually around the sample, producing a smaller image size of 506×1360×400, followed by the background subtraction with the 10 background images. After the cropping and background subtraction which normally take less than 1 second, the average time of each channel for COR correction and 3D reconstruction is 15.05s and 18.81s respectively with 5 nodes of 8-core 2.66 GHz CPU+ 16Gb RAM and 8 nodes of 4-core 2.66 GHz CPU+16Gb RAM, interconnected with a Gigabit Ethernet network. The number of selected sinograms is set as $\rho = 40$ to balance the effectiveness and computational complexity of COR localization, and the patch size is $w_1 = 15$. The visualizations of 3D reconstruction without and with the COR correction are shown in Fig. 7 (a), (b), (c) and Fig. 8 (a), (b), (c). It is obvious that Fig. 8 (a), (b) and (c) contain distinct signals in both channels while Fig. 7 (a), (b) and (c) show blurred 3D models and signals. 10 slices of cross-section image selected from the combination model in (c) are magnified in Fig. 7 (d) and Fig. 8 (d). It is obvious that Fig. 8 (d) accurately expressed the zebrafish spine and structural GFP1 fluorescence signals.

To quantitatively compare the difference between the reconstructed slices without and with COR correction, coefficient of variation (CV): $c_v = \frac{\sigma}{\mu}$ is calculated for each reconstructed slice as shown Fig. 7 (e) and Fig. 8 (e). It should be noted that the CVs calculated in our experiments are based on the raw data from reconstruction instead of the scaled gray images. In terms of reducing artifacts produced in the reconstruction, we aim to simultaneously maximize the variance and minimize the mean of bright-field and fluorescence signals, describing discriminate structure with the least blur. By comparing Fig. 7 (e) with Fig. 8 (e), we can see that after COR correction c_v increases significantly on all slices in both channels.

To observe more details in the reconstructed image slices, the histograms for the average image of the selected 10 slices without and with COR correction are illustrated in Fig. 7 (f) and Fig. 8 (f). The pixel value corresponds to the bright-field (in purple) or fluorescence (in blue) signal strength. In practice, the bright-field image is inverted to satisfy the correspondence of pixel value and signal strength. In Fig. 7 (f) and Fig. 8 (f), the peaks of the histogram indicate the pixel values of the background, and values for signals are on the right of the peak. It is obvious that the background boundary of the histogram (black arrow) in Fig. 8 (f) is sharper than that in Fig. 7 (f). The peaks in Fig. 8 (f) are both higher than peaks in Fig. 7 (f), proving that COR correction clears the background which is smeared by blurred artifacts. This is consistent with the refined and discriminate silhouette and texture of reconstructed image with COR correction.

To illustrate the over-all runtime of the pipeline, we repeat the experiments on 10 more data ranging from zebrafish and zebra-finch embryo to chicken embryo heart with different imaging magnifications. The parameters of COR correction and the configuration of parallel computing are set as the same as the experiments above. The only difference is that we fixed the image size as the original 1036×1360×400 pixels without cropping to exclude the influence of different image sizes on runtime. Fig. 9 describes the runtime

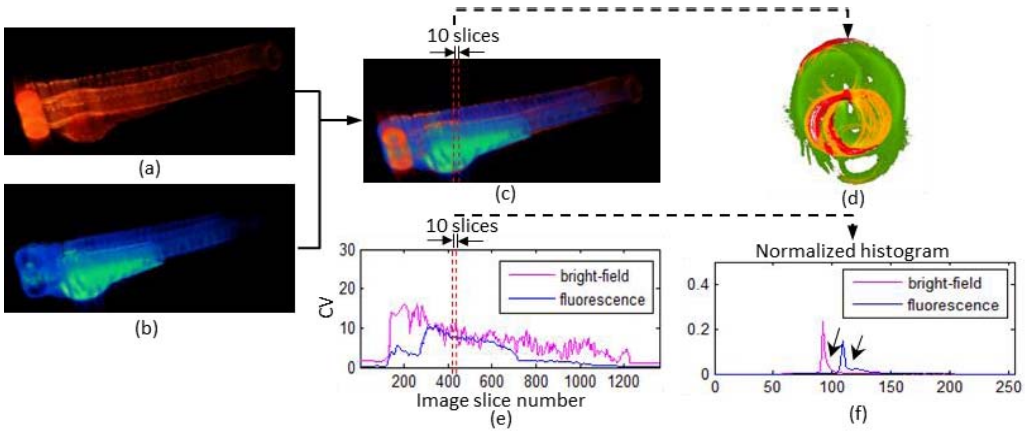

Fig. 7. An example of 3D reconstruction for a 3dpf zebrafish without COR calibration on hardware before imaging. The results are obtained based on the proposed pipeline without COR correction. (a), (b) 3D image in bright-field and Fluorescence channel. (c) The combination of (a) and (b). (d) Reconstructed slices between 410 and 419 of (c). The bright-field and fluorescence signals are shown in red and green and the intersections of them are in yellow. (e) The coefficient of variation of all slices corresponding to (c). (f) Normalized histograms for the average of the 10 slices selected from (c) and (e). black arrows indicate the statistical characteristics of the reconstructed silhouette for the zebrafish.

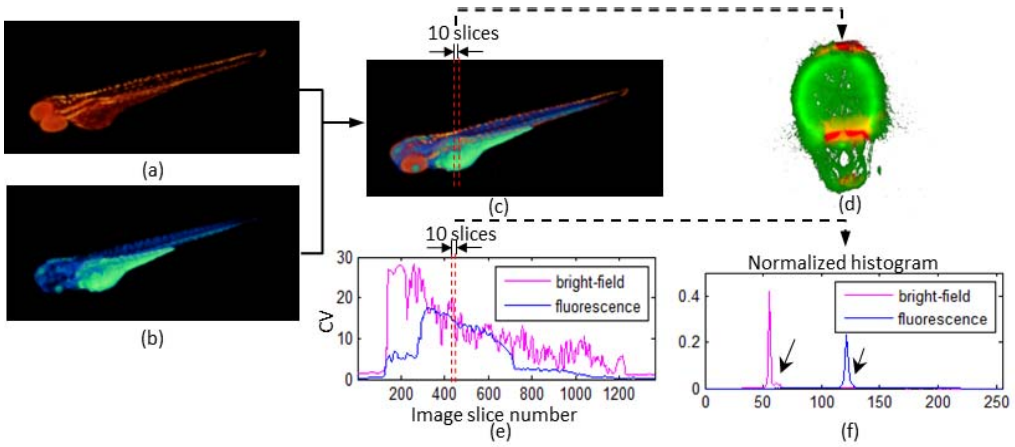

Fig. 8. 3D reconstruction for the 3dpf zebrafish without COR calibration on hardware before imaging, but the results are compensated with the proposed pipeline with COR correction. (a), (b) 3D image in bright-field and Fluorescence channel. (c) Combination of (a) and (b). (d) Reconstructed slices between 410 and 419 of (c). The bright-field signals (in red) describe the distinct spine of the zebrafish. The fluorescence signals (GFP1) are shown in green and the brightness of color indicates the strength of GFP1, decribing the fluorescence texture. (e) coefficient of variation of all slices corresponding to (c). (f) Normalized histograms for the average of the 10 slices selected from (c) and (e). The peaks (background) are higher and the edges (blak arrow) are shaper than those in Fig. 7 (f).

of 3D reconstruction (Rec) and that of 3D reconstruction with COR correction (Rec&COR). Over all, Rec takes average time of 26.91s and Rec&COR takes 54.66s on the tested 10 dataset.

B. Comparison of Different COR Corrections on Different Data

Three previous COR correction approaches are analyzed and compared to the proposed method on the 12 OPT images. The Pixel Match method and the Cross Correlation Operation (CCO) method [22] are based on signal match for pairs of projection, both of which are successfully used in CT COR correction. The most commonly used method in OPT COR correction is the one proposed in [24], named as Automatic method in this paper. We name the COR correction algorithm proposed in this paper as the Interest Point Based (IPB) method. As the results of COR correction depend on the selection of sinograms, the comparisons of different COR correction methods are implemented on multiple sinograms selected with the proposed strategy above. For the 12 OPT image dataset, we choose both the organism and organs from different stages for the experiments, including zebrafish embryo (ZE), chicken embryo heart (CEH) and zebra finch embryo (ZFE) in bright-field (B) and fluorescence (F) channel. The research related to these data involves embryo and skeleton development in the early growth of the specimens.

As the results indicated in Fig. 10, the measurement of CV considers both the variance and mean of the reconstructed results, which are more convincing and reliable. The data used for CV calculation is also the raw data after reconstruction before image normalization, excluding the effect of scaling. We should keep in mind that CV is only the criteria for evaluating the performance of different reconstruction of the same specimen. It is not suitable for comparing the reconstruction

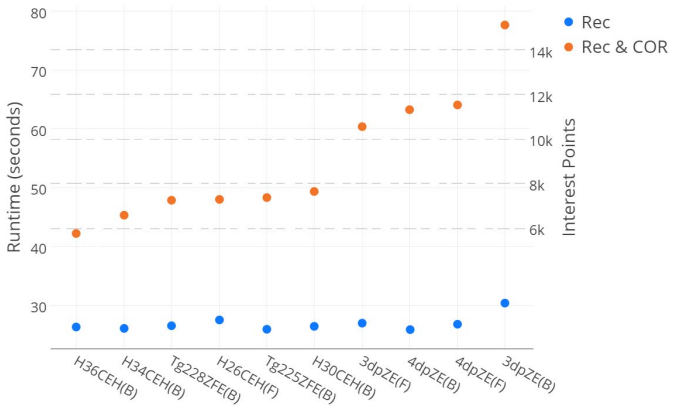

Fig. 9. The runtime (solid axis) of the pipeline implemented on the cluster. Rec represents the runtime for 3D reconstruction and Rec&COR indicates the runtime including COR correction as well. The increasing runtime of REC&COR corresponds to the increasing number of interest points (dashed axis) detected in the COR correction algorithm on different data.

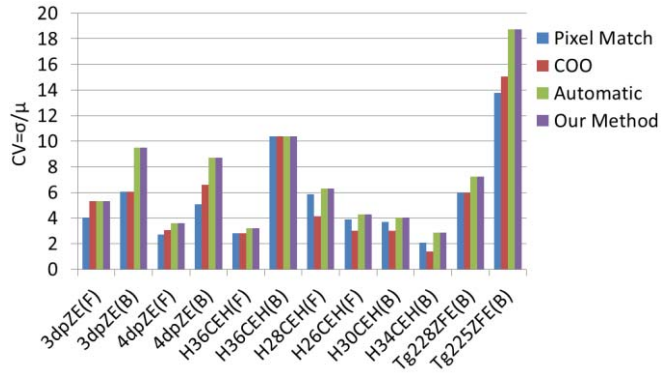

Fig. 10. The comparison of average coefficient of variation (CV) for reconstruction with 4 different COR correction methods on 12 datasets. For each dataset, larger CV corresponds to discriminate information and less artefacts introduced by reconstruction. ZE is short for zebrafish embryo; CEH is for chicken embryo heart; ZFE represents zebra finch embryo; Different prefixes refer to different stages when specimens were imaged. B and F are the bright-field and fluorescence channel.

performance across specimens, because the variance and mean value differs in different specimen structures. But for the same specimen, CV is more promising for evaluating reconstruction performance than variance in [24]. In Fig. 10, the Automatic method [24] and IPB obtained the maximum CV on all the 12 datasets, because both methods achieved the optimal and equivalent COR on each dataset. The Pixel Match [21] and CCO methods [22] gained different reconstruction and CV performance on different data. The reason for this variety is that the algorithms in [21] and [22] strongly depend on the symmetry of all oppositely projected pixel pairs. But in the practical OPT imaging, most of the pairs are not symmetrical.

Apart from the competitive performance of reconstruction quality with the Automatic method in Fig. 10, IPB method performs significantly superior to CCO method and Automatic method in terms of its computational complexity; cf. Table 1. With the computer configuration of 16Gb RAM and 8-core 3.4 GHz CPU, the average runtime

TABLE I
RUNTIME OF DIFFERENT COR ALIGNMENT APRROACHES IN EACH SINOGRAM ON DIFFERENT DATASETS

Datasets	Pixel Match(s)	CCO(s)	Automatic(s)	Ours(s)
3dpf ZE (F)	0.6897	102.8966	1043.1034	10.3448
3dpf ZE (B)	0.6765	102.7941	1042.7941	12.2941
4dpf ZE (F)	0.6897	102.9310	1043.3793	11.7241
4dpf ZE (B)	0.6786	102.8929	1042.8214	11.7241
HH36 CEH (F)	0.6774	102.9032	1043.2580	2.2258
HH36 CEH (B)	0.6667	102.9333	1042.8444	6.2888
H28 CEH (F)	0.6800	103.1200	1043.1200	5.2000
H26 CEH (F)	0.7200	103.2000	1043.2000	4.3200
H30 CEH (B)	0.6774	103.5484	1043.1935	4.1612
H34 CEH (B)	0.6897	103.5517	1043.0344	3.3793
Tg228 ZFE (B)	0.7143	103.1786	1042.8571	2.6785
Tg225 ZFE (B)	0.7857	103.2143	1042.7857	2.7857
Average	**0.6955**	**103.097**	**1043.0326**	**6.4272**

of different COR correction methods for single sinogram are 0.6955s, 103.097s, 1043.0326s and 6.4272s respectively. The Pixel Match method [21] achieves highest performance in runtime, but its capability of optimal COR correction is inadequate. Overall, IPB outperforms the other three by considering the effectiveness as well as computational complexity. It is noteworthy that the runtime of different dataset using IPB varies due to the differences of the number of interest points; while other three approaches consume approximately the same fixed runtime for each sinogram because they considered a fixed number of sinogram pixels.

IV. CONCLUSION

In this paper we presented the fast post-processing pipeline for 3D the reconstruction on OPT, as well as a new automatic COR correction method outperforming other three COR correction approaches in terms of general efficiency. We implemented the pipeline based on parallel computation and the average runtime based on the 10 datasets with the fixed image size of $1036 \times 1360 \times 400$ is 54.66s, when using 5 nodes of 8-core 2.66 GHz CPU+16G RAM and 8 nodes of 4-core 2.66 GHz CPU+16G RAM. Furthermore, the proposed COR correction methodology could suppress random or fixed noise in background, because only peaks and troughs of the sinogram from foreground are detected as interest points. Importantly, the proposed pipeline and COR correction are also suitable for 3D CT image reconstruction and comparison when tracking medical therapy. Currently, the integrated system including imaging, data transfer, preprocessing, COR correction, 3D reconstruction and visualization is being optimized as a distributed application on a cluster. With this integrated system, the profile of the organism/organ and fluorescence probes within it can be imaged, reconstructed and 3D visualized within several minutes. Moreover, a quantitative model for locating, calculating and tracking fluorescence signals (gene and/or protein activity) will be established in our future work.

ACKNOWLEDGMENT

The authors thank Dr Monique Welten for providing images of zebra-finch for development research.

REFERENCES

[1] J. Sakurai, A. Ahamed, M. Murai, M. Maeshima, and M. Uemura, "Tissue and cell-specific localization of Rice aquaporins and their water transport activities," *Plant Cell Physiol.*, vol. 49, no. 1, pp. 30–39, 2008.

[2] E. B. Brown *et al.*, "*In vivo* measurement of gene expression, angiogenesis and physiological function in tumors using multiphoton laser scanning microscopy," *Nat. Med.*, vol. 7, no. 7, pp. 864–868, 2001.

[3] L. Quintana and J. Sharpe, "Optical projection tomography of vertebrate embryo development," *Cold Spring Harbor Protocols*, vol. 6, no. 6, pp. 586–594, 2011.

[4] S. Z. M. Muji *et al.*, "Optical tomography: A review on sensor array, projection arrangement and image reconstruction algorithm," *Int. J. Innov. Comput. Inf. Control*, vol. 7, no. 7A, pp. 3839–3856, 2011.

[5] J. Sharpe *et al.*, "Optical projection tomography as a tool for 3D microscopy and gene expression studies," *Science*, vol. 296, no. 5567, pp. 541–545, 2002.

[6] W. Denk, J. H. Strickler, and W. W. Webb, "Two-photon laser scanning fluorescence microscopy," *Science*, vol. 248, no. 4951, pp. 6–73, 1990.

[7] S. Ogawa, T. M. Lee, A. R. Kay, and D. W. Tank, "Brain magnetic resonance imaging with contrast dependent on blood oxygenation," *Proc. Nat. Acad. Sci. USA*, vol. 87, no. 24, pp. 9868–9872, 1990.

[8] J. Michálek and M. Capek, "Artifact-free 3D reconstruction for optical projection tomography," *Microscopy Microanal.*, vol. 20, no. S3, pp. 1362–1363, 2014.

[9] M. Singh *et al.*, "Comparison of optical projection tomography and optical coherence tomography for assessment of murine embryonic development," *Proc. SPIE* pp. 93340J-1–93340J-8, Mar. 2015.

[10] S. Kumar *et al.*, "Quantitative *in vivo* optical tomography of cancer progression & vasculature development in adult zebrafish," *Oncotarget*, vol. 5, no. 28, pp. 2–11, 2016.

[11] Q. Miao *et al.*, "Dual-mode optical projection tomography microscope using gold nanorods and hematoxylin-stained cancer cells," *Opt. Lett.*, vol. 35, no. 7, pp. 1037–1039, 2010.

[12] N. Agarwal, A. M. Biancardi, F. W. Patten, A. P. Reeves, and E. J. Seibel, "Three-dimensional DNA image cytometry by optical projection tomographic microscopy for early cancer diagnosis," *J. Med. Imag.*, vol. 1, no. 1, p. 17501, 2014.

[13] J. McGinty *et al.*, "*In vivo* fluorescence lifetime optical projection tomography," *Biomed. Opt. Exp.*, vol. 2, no. 5, pp. 1340–1350, 2011.

[14] L. Fieramonti *et al.*, "Time-gated optical projection tomography allows visualization of adult zebrafish internal structures," *PLoS One*, vol. 7, no. 11, p. e50744, 2012.

[15] A. Bassi, L. Fieramonti, C. D'Andrea, M. Mione, and G. Valentini, "*In vivo* label-free three-dimensional imaging of zebrafish vasculature with optical projection tomography," *J. Biomed. Opt.*, vol. 16, no. 10, p. 100502, 2011.

[16] M. Y. Beebeejaun, P. Sharpe, and S. Pacheco, "3-D reconstruction of tooth development and gene expression using optical projection tomography," *J. Mol. Imag. Dyn.*, vol. 2, no. 1, pp. 1–5, 2012.

[17] T. Correia *et al.*, "Accelerated optical projection tomography applied to *in vivo* imaging of zebrafish," *PLoS One*, vol. 10, no. 8, p. e0136213, 2015.

[18] S. G. Azevedo, D. J. Schneberk, J. Fitch, and H. E. Martz, "Calculation of the rotational centers in computed tomography sinograms," *IEEE Trans. Nucl. Sci.*, vol. 37, no. 4, pp. 1525–1540, Aug. 1990.

[19] B. Zitová and J. Flusser, "Image registration methods: A survey," *Image Vis. Comput.*, vol. 21, pp. 977–1000, Oct. 2003.

[20] B. Olander, "Centre of rotation determination using projection data in X-ray micro computed tomography," Dept. Radiol., Linköping Univ., Linköping, Sweden, Tech. Rep. 77, 1994.

[21] K. B. Jan, "3D computed tomography," Czech Techn. Univ., Praha, Czechia, Tech. Rep., 2004.

[22] Y. Min, G. Haidong, L. Xingdong, M. Fanyong, and W. Dongbo, "A new method to determine the center of rotation shift in 2D-CT scanning system using image cross correlation," *NDT E Int.*, vol. 46, pp. 48–54, Mar. 2012.

[23] A. Brunetti and F. De Carlo, "A robust procedure for determination of center of rotation in tomography," *Proc. SPIE*, pp. 652–659, Oct. 2004.

[24] T. Donath, F. Beckmann, and A. Schreyer, "Automated determination of the center of rotation in tomography data," *J. Opt. Soc. Amer. A, Opt. Image Sci.*, vol. 23, no. 5, pp. 1048–1057, 2006.

[25] J. R. Walls, J. G. Sled, J. Sharpe, and R. M. Henkelman, "Correction of artefacts in optical projection tomography," *Phys. Med. Biol.*, vol. 50, no. 19, pp. 4645–4665, 2005.

[26] X. Tang *et al.*, "Fluorescence and bright-field 3D image fusion based on sinogram unification for optical projection tomography," in *Proc. IEEE Int. Conf. Bioinformat. Biomed. (BIBM)*, Jun. 2016, pp. 403–410.

[27] N. Otsu, "A threshold selection method from gray-level histograms," *IEEE Trans. Syst., Man, Cybern.*, vol. 9, no. 1, pp. 62–66, Jan. 1979.

[28] I. Sobel and G. Feldman, "A 3×3 isotropic gradient operator for image processing," *Talk Stanford Artif. Project Pattern Classification Scene Anal.*, pp. 271–272, 1968.

[29] A. C. Kak, M. Slaney, and G. Wang, "Principles of computerized tomographic imaging," *Med. Phys.*, vol.29, no. 1, p. 107.

Xiaoqin Tang received the bachelor's and master's degrees from Southwest University, China, with research background of machine learning and action recognition in video. She is currently pursuing the Ph.D. degree with the Imaging and Bioinformatics Group, Leiden Institute of Advanced Computer Science, Leiden University, The Netherlands. Her current research interests include acquiring optimized 3-D reconstructed images to help the biologists identify and localize protein and/or gene in samples, such as zebrafish and shark embryos, using the OPT imaging system.

Dennis M. van der Zwaan received the B.S. degree in computer science from Leiden University in 2016, where he is currently pursuing the M.S. degree in computer science. His research interests include high performance computing, artificial intelligence, and user experience research.

Alan Zammit received the B.Sc. degree in computer science from the University of Malta in 1994. He is currently pursuing the master's degree in computer science with the Leiden Institute of Advanced Computer Science. He has 20 years' experience in the IT industry. Within the Imaging and Bioinformatics Group, his primary research focus is on high-performance image processing pipelines.

Kristian F. D. Rietveld received the Ph.D. degree in computer science from Leiden University, The Netherlands, in 2014. He is currently a Lecturer in computer systems with the Leiden Institute of Advanced Computer Science. His research interests include parallel and distributed computing, optimizing compilers, program transformation, and database systems.

Fons J. Verbeek received the Ph.D. degree in applied physics (pattern recognition group) from the Delft University of Technology, The Netherlands, in 1995. He is currently chairing the Imaging and Bioinformatics Group with the Leiden Institute of Advanced Computer Science, Leiden University, The Netherlands. In his group, the research interests include the development of robust methods for large-scale image processing and analysis in the biosciences and the zebrafish model system is used in a range of different application areas.